Lithium-Ion Battery Degradation: Measuring Rapid Loss of Active Silicon in Silicon-Graphite Composite Electrodes

Niall Kirkaldy [a]*, Mohammad Amin Samieian [a], Gregory J Offer [ab], Monica Marinescu [ab], Yatish Patel [a]*

[a] Department of Mechanical Engineering, Imperial College London, London, SW7 2AZ, United Kingdom
[b] The Faraday Institution, Harwell Science and Innovation Campus, Didcot, OX11 0RA, United Kingdom
* Corresponding authors' email addresses: n.kirkaldy@imperial.ac.uk & yatish.patel@imperial.ac.uk

Abstract

In an effort to increase the specific energy of lithium-ion batteries, silicon additives are often blended with graphite (Gr) in the negative electrode of commercial cells. However, due to the large volumetric expansion of silicon upon lithiation, these Si-Gr composites are prone to faster rates of degradation than conventional graphite electrodes. Understanding the effect of this difference is key to controlling degradation and improving cell lifetimes. Here, we investigate the effects of state of charge and temperature on the ageing of a commercial cylindrical cell with a Si-Gr electrode (LG M50T). Using degradation mode analysis, we were able to quantify the rates of degradation for Si and Gr separately. Loss of active Si is shown to be worse than Gr under all operating conditions, but especially at low state of charge and high temperature, with up to 80% loss in Si capacity after 4 kA h of charge throughput (~400 equivalent full cycles). The results indicate cell lifetimes can be improved by limiting the depth of discharge of cells containing Si-Gr, which suggests Si is not beneficial for all applications. The degradation mode analysis methods developed here provide valuable new insight into the causes of cell ageing by separating the effects of the two active materials in the composite electrode. These methods provide a suitable framework for data analysis of any experimental investigations on cells involving composite electrodes.

Keywords: Lithium-ion batteries, ageing, degradation modes, silicon, Si-Gr

Introduction

Enabled by their high energy density and specific energy, lithium-ion batteries (LIBs) have become the dominant energy storage technology for mobile applications. Average battery energy densities for electric vehicles (EVs) are rising at a rate of 7% per year.[1] In the near term, they are expected to reach values of 325 W h kg^{-1} at the cell-level, and 275 W h kg^{-1} at pack-level.[2] This has been made possible using new active materials in their construction, such as nickel-rich transition metal oxides like $LiNi_{0.8}Mn_{0.1}Co_{0.1}O_2$ (NMC811) on the positive electrode (PE), and by incorporating silicon additives into the (typically) graphite negative electrode (NE).

Silicon is viewed as a promising NE material for LIBs due to its large specific capacity, which is around 10 times greater than that of graphite (3579 mA h g^{-1} for $Li_{15}Si_4$ vs. 372 mA h g^{-1} for LiC_6).[3] Unlike intercalation materials such as graphite, silicon undergoes an alloying reaction upon lithiation. This leads to a significant volume expansion of over 300% in the fully-lithiated state, compared to graphite which expands by around 20% upon lithiation.[4,5]

This expansion and contraction of the electrode during charge and discharge of the cell results in mechanical stress on the electrode particles.[6] These stresses can cause particles to crack, or even become completely detached from the rest of the electrode (known as island formation). These electrically-isolated materials can no longer contribute to the capacity of the cell, hampering the performance.[7] The large volumetric changes also cause the solid electrolyte interphase (SEI) layer to

crack and become detached. This in turn leads to new electrode surfaces being exposed to the electrolyte, with additional SEI growth.[8] Even under calendar ageing conditions, SEI formation on Si is more dynamic and less passivating than that formed on graphite, leading to greater levels of degradation.[9,10] Due to these issues, lifetimes of pure Si electrodes are often too short to be relevant for commercial applications.[11]

Some of the negative effects of Si-based electrodes can be mitigated though blending silicon or silicon oxides (SiO_x) with other materials such as graphite. Silicon oxides undergo irreversible reduction reactions during the first lithiation cycle to form active silicon, inactive Li_2O and lithium silicates.[12–14] Silicon-graphite (Si-Gr) composite electrodes have been shown to drastically improve cell lifetimes.[10,13] Si-Gr electrodes with various structures and compositions have been explored to avoid the issues of electrical isolation and accelerated SEI growth.[15,16]

Due to the slightly higher oxidation potential of silicon vs. graphite in an LIB, the silicon portion of the composite Si-Gr electrode remains lithiated in all but the lowest states-of-charge (SoCs).[8,10] This means that cycling a cell at high SoC will largely utilise the graphite content of the NE, whereas cycling at low SoCs will use a greater proportion of the Si content.[16] Hence, the volumetric expansion of the silicon or graphite particles also depends on the SoC cycling range.[17] We therefore hypothesise that the rate of cell-level degradation will depend on the operational SoC window. We also expect the relative ageing rates of silicon and graphite in the NE vary with the SoC range.

Most degradation mechanisms in LIBs are in some way SoC (or potential) dependent;[18] mechanisms such as lithium-plating, SEI growth, and the various types of PE degradation are all exacerbated at higher cell SoC.[19–21] Similarly, the majority of degradation mechanisms are dependent on cell temperature and current (or C-rate).[20] Mechanisms which are caused by limited rates of Li^+ diffusion through the electrolyte and active material particles are generally aggravated by operating the cell at low temperatures or high C-rates.[21] This is due to slower transport at low temperature, and formation of concentration gradients at high C-rates.[22,23] Particle cracking is one such mechanism, since inhomogeneous lithiation will lead to greater strain on the active material particles, and hence to greater rates of degradation.[23]

Identifying which degradation mechanisms have contributed to the performance drop seen during battery ageing is a complex task. For verification of individual mechanisms, cell teardown must usually take place, with subsequent chemical, structural, and morphological analyses of the electrode and electrolyte.[7,24] However, the consequences of different degradation mechanisms can be grouped together based on their impact on the electrochemical performance of the cell. These groupings are termed degradation modes (DMs), and usually consist of loss of active material (LAM), loss of lithium inventory (LLI), and resistance increase (RI).[25] Each of these DMs can be quantified using in-situ, non-destructive electrochemical methods, without the need for the time-consuming, destructive ex-situ methods required for identifying mechanisms directly.[26,27]

DM analyses can be performed directly on voltage vs. capacity data,[27–29] or by using a derivative such as incremental capacity (dQ/dV)[25,30,31] or differential voltage (dV/dQ).[32–34] Various studies have shown that these methods can be used to identify which DMs have contributed to cell-level performance drop, both qualitatively and quantitatively. The same methods have been applied to cells which contain composite electrodes, such as Si-Gr.[35,36] Anseán *et al.* modelled the behaviour of a Si-Gr/NMC cell during ageing, and showed that the LAM of the two components of the NE can be decoupled, allowing insights into the way in which these composite electrodes age.[36] The profile of the NE voltage curve will change depending on the relative fractions of the two active materials, allowing insights into the way in which these composite electrodes age. This has since been confirmed experimentally

through cell teardown and electrode harvesting.[37] However, this composite electrode OCV-fitting method has never been used in experimental ageing studies to separately quantify the degradation contributions of silicon and graphite in Si-Gr composite electrodes.

With a range of commercial cells with Si-Gr negative electrodes recently becoming available, several experimental ageing studies have sought to understand how these composite electrodes influence cell degradation and lifetime.[7,38–40] These studies have provided valuable insight into the cell-level performance drop, and the influence of various operating conditions. However, most have relied on destructive cell teardown analyses, and none have managed to disentangle the degradation contributions made the two components of the NE. Here we seek to age commercial, Si-Gr containing cells with relevance to the EV industry by cycling over different SoC windows and temperatures. We investigate how these conditions affect degradation through traditional methods of capacity fade, resistance increase, and incremental capacity analysis (ICA). We expand on this by using the composite electrode OCV-fitting method to quantify which degradation modes occur during ageing. This allows us to quantify not just LLI and LAM of the PE and NE, but also LAM for both graphite and silicon. The resulting metrics provide a greater insight into the relative merits of Si in these commercial cells, with an apparent trade-off between increased capacity and reduced lifetime.

Experimental

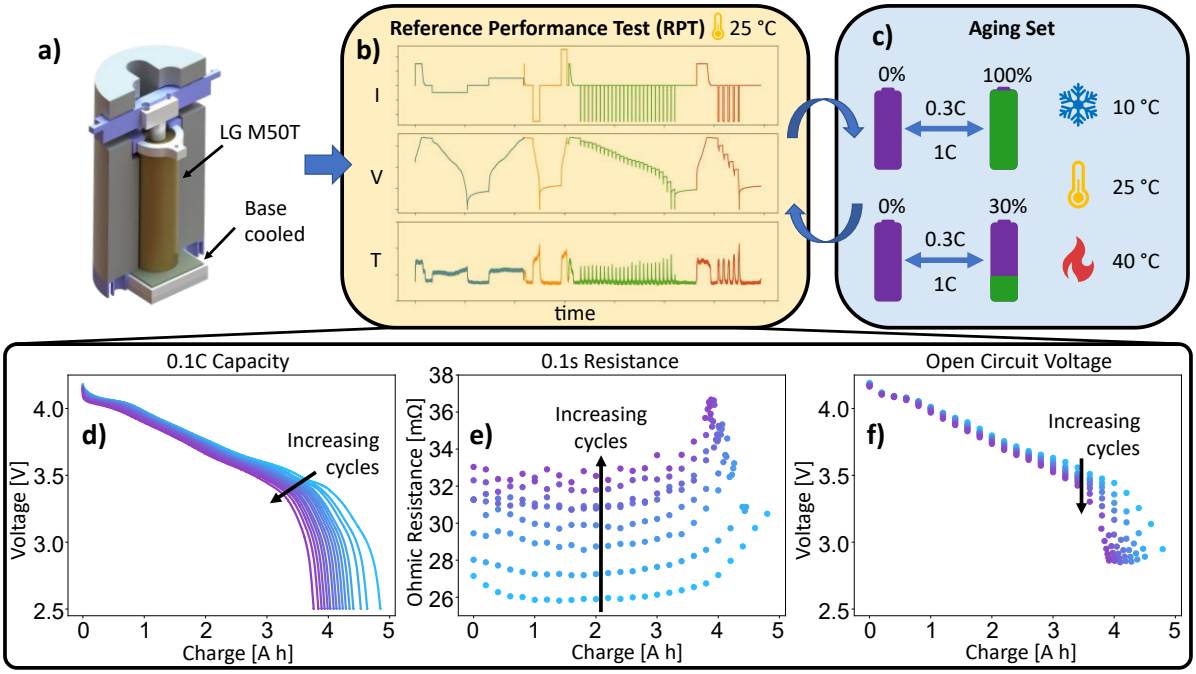

Figure 1: Schematic of the procedure used during this ageing study. a) diagram of the test apparatus for a single cell. b) Reference performance test used at BoL and after each ageing set. c) Conditions used during cycle ageing, with two SoC ranges and three temperature set-points. Cells were repeatedly subject to ageing sets and RPTs until they were deemed to have reached EoL. Example data for a single cell extracted from the RPT procedure, showing (d) 0.1C discharge capacity, (e) 0.1 second resistance, and (f) open circuit voltage.

In this study, we cycled a commercial 21700 cylindrical cell (LG M50T, LG GBM50T2170) at different temperatures and SoC ranges. The LG M50T is a high energy density commercial cell with relevance to the EV industry. These cells utilise a SiO_x-doped graphite negative electrode alongside an NMC-811 positive electrode and have a nominal capacity of 18.2 W h (5 A h).

Two sets of experiments were carried out. The first set of experiments involved cycling the cell over the full SoC range (0-100%), i.e. full depth-of-discharge (DoD). The second set of experiments

restricted the SoC to the low region (0-30%), where we expect to see greater rates of Si ageing. Both sets of experiments were performed at three different temperatures: 10°C, 25°C, and 40°C. The C-rates for charge (0.3C) and discharge (1C) were held constant throughout. A total of 17 cells were tested, distributed across the six experimental conditions (listed under the 'Ageing Sets' heading below). C-rates and capacities used for SoC control were based on the beginning-of-life (BoL) nominal capacity of 5 A h, i.e. 1C was equal to 5 A.

Apparatus

Cells were thermally managed using bespoke test rigs (Fig. 1a, and SI Figures S1, S2 & S3). In these test rigs, the base (negative end) of each cylindrical cell was in thermal contact with an aluminium block which was held at a constant set-point temperature using Peltier elements. The rest of the cell was wrapped in thermal insulation to minimise heat loss through surfaces other than the base of the cell. This setup effectively sets a constant temperature boundary condition on the base of the cell, with pseudo-adiabatic conditions on the other surfaces, and is inspired by the thermal management strategy used in some EVs.[41] Full details of the design of the test rigs can be found in the Supplementary Information (SI). The temperatures of the cells were measured using two K-type thermocouples (TCs) per cell: one was recorded using a Pico TC-08 data logger (sampling frequency of 0.2 Hz), the other was recorded by the battery cycler and used as a safety control. The TCs were adhered to the surface of the cell using Kapton tape, positioned halfway along the axial direction of the cell.

Both of the electrical connections were made via the top of the cell. Ring (negative) and pin (positive) terminals were pressed against the top of the cell using springs connected to the base of the test rigs. More details can be found in the SI. The terminals were connected to the battery cycler (Biologic BCS-815) current and voltage-sense cables via banana plugs. Cell impedance was tested after set-up by using the ZIR-compensation function of the BCS-815 at a frequency of 10 kHz and amplitude of 5 mV, averaging over 4 measurements. The total impedance (including ohmic resistance from the cell itself) was consistently found to be 27-30 mΩ; the cell itself was found to be 27 mΩ when measured using a 4-point connection, indicating the electrical connections added < 3 mΩ (all measured at 25°C). The resistance was not compensated for in subsequent tests.

Break-In Cycles

Once cells had been loaded into the test rigs, they were subject to five full discharge-charge cycles as part of the break-in procedure. This consisted of cycling cells between the upper and lower voltage limits (4.2 V and 2.5 V) using the standard charge and discharge procedures outlined on the manufacturer's specification sheet. These were a constant-current, constant-voltage (CC-CV) charge (with a C-rate of 0.2C until 4.2 V, and a 4.2 V hold until the current dropped below 0.01C), and a CC discharge (with a C-rate of 0.2C). Cells were rested under open-circuit conditions for 2 hours after each charge and 4 hours after each discharge. All break-in cycles were performed at 25°C.

Characterisation Procedure

After the break-in procedure was complete, the beginning-of-life (BoL) performance of the cells were measured using a reference performance test (RPT). Two different RPT procedures were used in this study: the longer RPT provided more information on the cell performance but took around 100 hours to complete; the shorter RPT provided less information but required around half the time. Both RPT procedures were performed at BoL, and used alternatingly after each ageing set. RPTs were always carried out at 25°C, enabling comparisons between cells which were aged at different temperatures. The details of the longer RPT procedure are listed below and displayed in Figure 1b. Full details of both procedures can be found in Table S1 & S2 of the SI.

The longer RPT can be broken down into four sub-tests, as indicated in the different coloured portions of Figure 1b. This consisted of i) a 0.1C discharge-charge (shown in blue in Fig. 1b), ii) a 0.5C discharge-charge (orange), and iii/iv) two galvanostatic intermittent titration technique (GITT) discharge tests performed at 0.5C. The first of these (subtest iii) comprised of 25 pulses, each passing 200 mA h of charge, with 1 hour rest periods between each pulse (green). The second (subtest iv) comprised of 5 pulses, each passing 1000 mA h of charge, also with 1 hour rest periods between pulses (red). In all cases, voltage limits of 4.2 V (upper) and 2.5 V (lower) were imposed to prevent over-charge/discharge. Prior to each of the four sub-tests, the cells were first charged using a standard CC-CV method, with a C-rate of 0.3 C until 4.2 V, and a 4.2 V hold until the current dropped below 0.01C. The cells were then rested under open-circuit conditions for 2 hours to allow the voltage and temperature to equilibrate. Upon reaching the 2.5 V lower voltage limit on discharge, cells were rested under open-circuit conditions for 6 hours prior to commencing the next part of the procedure. The long rest periods were required due to the slow relaxation of these cells at low SoCs.

Ageing Sets

Once the BoL characterisation was complete, the cells were brought to the temperature set points required for their ageing cycles and allowed to thermally equilibrate for 2 hours. Two different SoC ranges were used in this study: 0-30% and 0-100% SoC. For each SoC range, three different temperature conditions were investigated: 10°C, 25°C, and 40°C. Details of the cycling conditions are shown in Table 1 for the 0-30% SoC and Table 2 for the 0-100% SoC range.

Table 1: Cycling conditions used for Experiment 1 (0-30% SoC cycling). Blue boxes indicate a looped section.

Step	Control Type	Control Value	Primary Limits	Cell SoC after completion	Safety Limits
1	CC discharge	1C	E_{cell} = 2.5 V	(0+x)%	E_{cell} = 2.5 V
2	CV discharge	2.5 V	$\|I\|$ < 0.01C	0%	N/A
3	Rest	Rest at OCV	time = 4 hours	N/A	N/A
4	CC charge	0.3C	Q = 1500 mAh (=capacity$_{BoL}$*0.3)	30%	E_{cell} = 4.2 V
5	CC discharge	1C	E_{cell} = 2.5 V	0%	E_{cell} = 2.5 V
6	Loop to step 4	N/A	257 times	N/A	N/A

Table 2: Cycling conditions used for Experiment 2 (full depth-of-discharge). Blue boxes indicate a looped section.

Step	Control Type	Control Value	Primary Limits	Cell SoC after completion	Safety Limits
1	CC charge	0.3C	E_{cell} = 4.2 V	(100-y)%	E_{cell} = 4.2 V
2	CV charge	4.2 V	$\|I\|$ < 0.01C	100%	N/A
3	Rest	Rest at OCV	time = 4 hours	N/A	N/A
4	CC discharge	1C	E_{cell} = 2.5 V	0%	E_{cell} = 2.5 V
5	CC charge	0.3C	E_{cell} = 4.2 V	(100-y)%	E_{cell} = 4.2 V
6	CV charge	4.2 V	$\|I\|$ < 0.01C	100%	N/A
7	Loop to step 4	N/A	77 times	N/A	N/A

The ageing sets described in Table 1 and 2 consist of a set number of charge-discharge cycles. To maintain a fair comparison between the cells aged under different SoC windows, the number of cycles performed in each case was scaled to be equivalent in terms of number of full cycles. This meant that the full DoD (0-100% SoC) ageing set had approximately 0.3 times the number of cycles of the 0-30%

SoC ageing set. After each set of ageing cycles, cells were brought to 25°C and the performance of the cells were measured in another RPT. This process continued until the cells were deemed to have reached end of life (EoL).

The C-rates and capacities used for control of the SoC windows were not de-rated as the cells aged, with the nominal BoL capacities used throughout. A consequence of using coulomb-counting as the control method in the 0-30% SoC range cycling is that the voltage window over which the cell is cycled increases as the cell degrades, since the capacity used for setting the charge limit was not de-rated. Conversely, the cells cycled over the 0-100% SoC range are controlled by voltage set points, meaning the charge passed during each ageing set will decrease as the cells degrade. These are unavoidable issues with ageing studies of LIBs, but the impact on the results can be minimised through comparing against charge throughput rather than cycle number, as discussed below.

Analysis Methods

All analyses of the electrochemical data were performed using Python, making use of the Pandas, Numpy, Scipy, and Matplotlib libraries. Measurements of charge throughput were taken from the ageing cycle data; this corresponds to the total measured charge passed during the ageing cycles (from both charge and discharge sections). Charge throughput is used in subsequent analyses instead of 'number of equivalent full cycles', since the charge passed in each cycle decreases as the cells age. Aside from the measure of charge throughput, all other information used in the rest of the analyses utilise data from the RPTs.

Cell capacity measurements were taken from the 0.1C discharge cycle performed in each RPT (e.g. Fig. 1d), from which 'capacity fade' was calculated using the following equation:

$$\text{Capacity Fade } (\%) = \frac{\text{Capacity}_{0.1\text{C,BoL}} - \text{Capacity}_{0.1\text{C}}}{\text{Capacity}_{0.1\text{C,BoL}}} \times 100 \qquad (1)$$

The ohmic resistance of the cells were calculated using the 25-pulse GITT data, from the instantaneous voltage drop upon application of the current pulse, as:

$$\text{Ohmic Resistance } (\Omega) = \frac{V_2 - V_1}{I_2 - I_1} \qquad (2)$$

where I_1 and V_1 are the current and voltage at rest before application of the current pulse, and I_2 and V_2 are the values immediately after current is applied. The sampling rate for these measurements was 10 Hz, so the 'instantaneous' voltage drop is approximated as that measured after 0.1 seconds. At this response time, only minor contributions from resistances other than ohmic (i.e. activation/charge transfer) are expected.

This procedure was repeated for each pulse in the GITT tests, giving ohmic resistance as a function of SoC (as shown in Fig. 1e). The increase in ohmic resistance with ageing was tracked for the resistance value thus obtained from the 12th pulse of the procedure (equating to ~52% SoC using the nominal BoL capacity). This value was chosen due to the relative plateau in the BoL resistance values over the central SoC range of the cell. As with the capacity, the increase was defined relative to the BoL values:

$$\text{Resistance Increase } (\%) = \frac{\text{Ohmic Resistance} - \text{Ohmic Resistance}_{\text{BoL}}}{\text{Ohmic Resistance}_{\text{BoL}}} \times 100 \qquad (3)$$

Incremental capacity analysis (ICA) was performed using the 0.1C discharge and charge cycle by differentiating the cell capacity with respect to voltage using a finite-difference method, with a set dV of 5 mV. Prior to this, the measured capacity was normalised using the nominal BoL capacity (5 A h)

to give a measure of SoC. The differentiated data is therefore termed d*SoC*/d*V*. No smoothing was performed on the data.

Degradation Mode (DM) analysis was performed using the 0.1C discharge data. Half-cell *V* vs *Q* datasets were also required for this analysis, which were taken from the literature.[14,29,42] This consisted of BoL data from the positive electrode, as well as separate datasets for each of the two components of the negative electrode (Gr and Si).

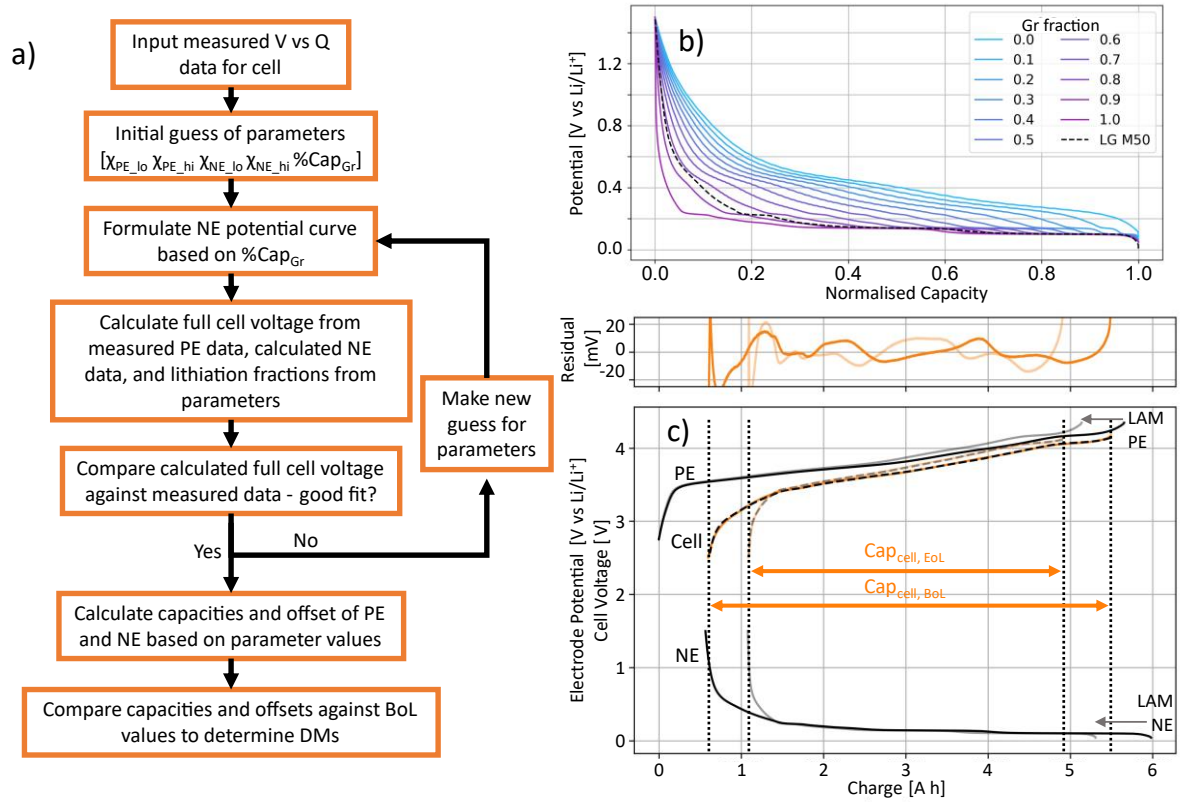

Figure 2: OCV-fitting procedure for quantifying the degradation modes. a) Procedure for fitting the measured cell V vs Q data to a calculated V vs Q curve. b) A potential curve of the NE is formulated based on measured potential curves of Gr and Si and the relative ratio of the two components in the NE. c) An experimentally measured potential curve of the PE is used together with the NE potential curve in (b) to calculate a full-cell voltage curve based on the upper and lower lithiation fractions of each electrode. By repeating at each stage of SoH, degradation modes of LAM-PE, LAM-NE, LAM-NE-Gr, LAM-NE-Si, and LLI can be determined based on the change in the electrode capacities and offset. In c) the BoL data is depicted by dark lines, with data from an aged cell depicted by faded lines. The measured full cell data is shown in orange, with the calculated full cell data shown in black dashed lines. The residual between the measured and calculated full cell curves is shown above as a function of the cell capacity. All datasets correspond to cell discharge, i.e. lithiation of the PE and delithiation of the NE.

We first investigated if the two components of the NE could be used to reproduce the measured half-cell voltage curve of the composite NE. The capacity of the NE at any given voltage is the sum of the capacity available in the two components:

$$Q_{composite}(\mathrm{V}) = Q_{Gr}(\mathrm{V}) + Q_{Si}(\mathrm{V}) \tag{4}$$

$$Q_{composite} = Q_{composite} \times \%Cap_{Gr} + Q_{composite} \times \%Cap_{Si} \tag{5}$$

$$\%Cap_{Gr} + \%Cap_{Si} = 1 \tag{6}$$

where $Q_{composite}$, Q_{Gr} and Q_{Si} are the capacities of the composite electrode, the graphite component, and the Si component, respectively. $\%Cap_{Gr}$ and $\%Cap_{Si}$ correspond to the relative fraction of the electrode capacity due to Gr and Si, respectively. Since the capacity of the composite electrode is

solely due to these two components, $\%Cap_{Gr}$ and $\%Cap_{Si}$ sum to unity. This means $\%Cap_{Si}$ can be expressed as $(1 - \%Cap_{Gr})$, allowing us to fit the component curve by adjusting only one parameter, $\%Cap_{Gr}$. It should be noted that equation 4 is valid only in the thermodynamic limit due to differing overpotentials present on the two components of the electrode. As such, it may only be suitable for low current measurements (near equilibrium). This limitation can be overcome by introducing current-dependent half-cell data for each component.[36]

Adjusting the relative contributions of each component (i.e. $\%Cap_{Gr}$) alters the calculated Q vs V curve of the composite electrode (Figure 2b). A non-linear least squares fitting procedure was run using the Gr and Si datasets alongside a measured V vs Q curve of the NE at BoL (SI Figure S7). This was done using the curve_fit() function within Scipy, using a Trust Region Reflective algorithm. From the resultant fit, we found the relative composition of the NE (in terms of capacity) to be 0.85 Gr : 0.15 Si at BoL (SI Figure S7). More information on the fitting procedure and error of the fit can be found in the SI.

The voltage curves of the two components were shown to accurately describe the composite electrode voltage, such that they can be used these data in the OCV-fitting method outlined in previous works and detailed in Figure 2a.[29] In this method, the capacities and offset between the PE and NE potential curves are adjusted by varying the upper and lower lithiation fractions of each (χ_{PE_lo}, χ_{PE_hi}, χ_{NE_lo}, χ_{NE_hi}). These four parameters are adjusted during a non-linear least squares fitting procedure similar to that described above, until the error between the calculated and measured full cell voltage curves is minimised.

The method is modified here to used two separate potential curves for the NE. The addition of the second NE curve adds in one more fitting parameter into the optimisation process, corresponding to the relative composition of Gr and Si in the NE ($\%Cap_{Gr}$, as described above). This means a new version of the composite NE potential curve is calculated for each iteration of the fitting procedure. Therefore, the results of the OCV-fitting now also include this new term, $\%Cap_{Gr}$. This allows us to quantify the capacities of the graphite and silicon content of the NE, and how they evolve with ageing. We can therefore calculate not just LAM-PE and LAM-NE, but also LAM-NE-Gr and LAM-NE-Si.

Results

The various sections of the RPT procedure allow us to extract different pieces of information on the cells' degradation behaviour. From the 0.1C cycle, we can take a good estimate of the cell capacity. As described in Eq. 1, we can calculate the capacity fade as a function of charge throughput during the ageing cycles. Figure 3a & b show the capacity fade of each cell, normalised against their BoL capacities.

The variance between cells was relatively low, with multiple repeats under each condition giving similar results (Figure 3a & b). The largest variance was observed when operating at low temperature (10°C), with lower spreads seen at the mid (25°C) and high (40°C) temperatures. Overall, at 25°C and 40°C, lower rates of degradation were seen when operating over the 0-100% SoC range compared to the 0-30% SoC range. However, this is an incomplete story since different relationships are observed in the initial 'accelerated ageing' region and the latter 'linear ageing' region. Low SoC cycling gives a greater initial capacity drop during the first 2 kA h of charge throughput, before a slower linear capacity fade thereafter (Fig. 3a). Conversely, full DoD cycling shows a smaller initial capacity drop, but the linear ageing region progresses at a faster rate, evident from the steeper gradient (Fig. 3b). In both the 0-30% and 0-100% SoC ranges, there is only a small difference between the observed capacity-fade behaviour at 25°C and 40°C. However, there is a stark difference when operating at

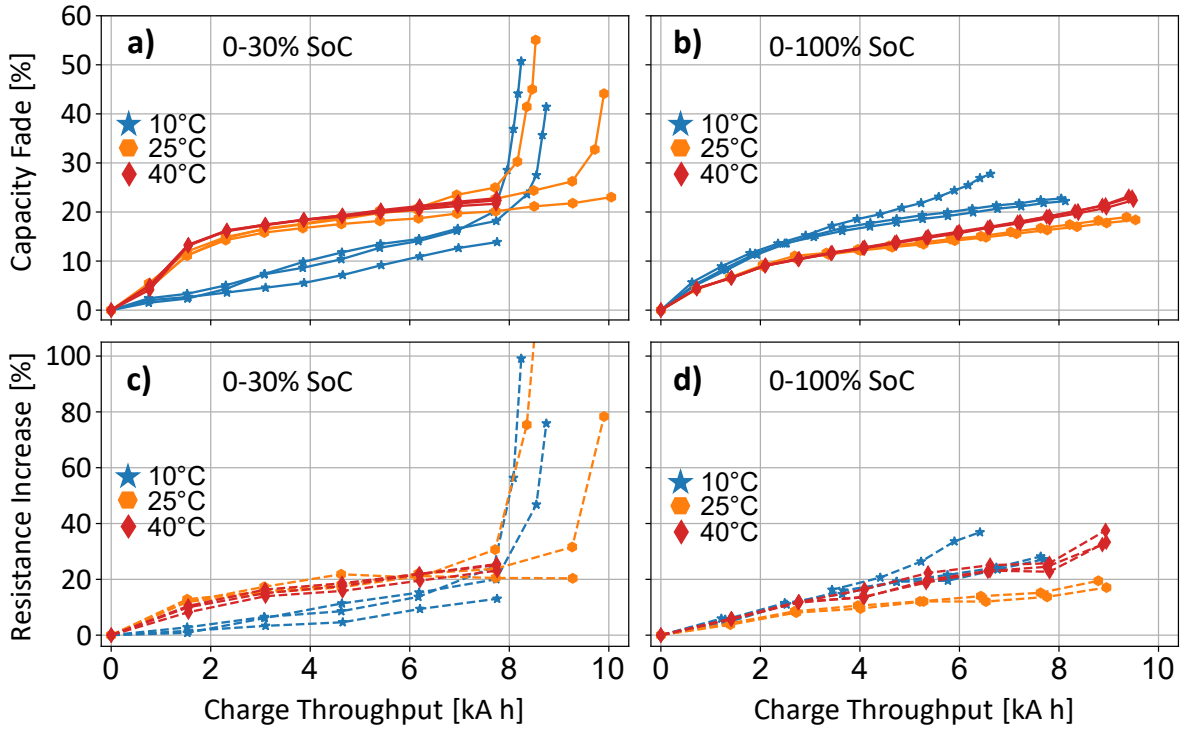

Figure 3: Capacity fade (a & b) and ohmic resistance increase (c & d) vs charge throughput for cells cycled at SoC ranges of 0-30% (a,c), and 0-100% (b,d). Colours correspond to the temperature at which the cells were aged (10°C blue stars, 25°C orange hexagons, and 40°C red diamonds). Each line corresponds to an individual cell tested, showing the repeatability of cells aged under the same conditions. Capacities taken from 0.1C discharge at each point shown, ohmic resistances calculated from GITT measurements.

10°C. In the 0-100% SoC cycling, the cells at 10°C age the fastest. The opposite behaviour is seen in the cells cycled between 0-30% SoC, with the cells aged at 10°C showing the lowest capacity fade for the first 7 kA h of charge throughput. As with the cells aged at warmer temperatures, the capacity-fade curve can be broken into two regions. The initial capacity fade seen during the 'accelerated' stage appears to be extremely low, but the rate of degradation seen in the 'linear' region is considerably higher than that seen at higher temperatures.

The ohmic resistance increase follows a similar trend to the capacity fade discussed above (Fig. 3c & d). A decrease in capacity could result in an apparent increase in ohmic resistance. This is due to a decrease in the electrochemically-active area of the electrode(s) whilst maintaining a constant resistivity. Conversely, resistance increase can cause a reduction in the useable capacity of a cell due to premature activation of the voltage cut-off limits upon charge or discharge. However, since the capacity measurements were performed at a low rate of 0.1C, the effect of the ohmic resistance increase on the measured capacity is relatively small. At 0.1C (500 mA), an increase in ohmic resistance of 20% (~5 mΩ) adds only 2.5 mV of overvoltage. This does not include overvoltages caused by an increase in the dynamic (or 'Faradaic') resistances. However, due to the steep gradient of the V vs Q plots at low SoC, the amount of capacity 'lost' through prematurely reaching the lower cut-off voltage is expected to be minimal.

Incremental capacity analysis (ICA) is a useful method for highlighting changes in the cell voltage during ageing. When performed on close-to-equilibrium data (i.e. low current), it can provide invaluable insight into the changes of the electrode compositions and capacities. Each peak in an ICA spectrum corresponds to a plateau in the voltage vs capacity (or SoC) profile.[25] For full cell data, a

plateau on the voltage vs capacity profile arises due to an overlap between the plateaux of the constituent half-cell profiles. Hence, peaks on an ICA spectrum do not correspond to processes/features of any single electrode, but instead to a combination of the features of the two electrodes.

Figure 4 shows the progression of the ICA spectra as the cells degrade, with data shown for one cell aged under each experimental condition. Fig. 4a-c correspond to cells cycled under the 0-30% SoC range, and Fig. 4d-f to cells cycled under the 0-100% SoC range. The different colours within each plot correspond to a 0.1C (dis)charge cycle performed during each RPT, from BoL (light blue) to EoL (dark purple), with approximately 77 equivalent full cycles between each consecutive RPT. Data for all cells can be found in SI Figures S8 & S9.

As discussed above, the peaks in an ICA plot cannot be attributed to one electrode. However, the peaks which correspond to (de)lithiation of silicon (alongside some PE feature) are principally observed in the low voltage region. In particular, we attribute the broad, short negative peak between 2.7-3.3 V, and the corresponding positive shoulder peak observed around 3.4 V to Si processes (inset, Fig. 4c).[36] These features rapidly disappear with increasing number of ageing cycles, in particular for the cells aged in the low SoC range (Fig. 4a-c). As cells approach EoL, a dramatic collapse of all features in the ICA profiles can be observed, as demonstrated by the cell aged at 0-30% SoC and 10°C (Fig. 4a). The point at which this phenomenon is observed correlates to the 'cliff-edge' moment for capacity fade shown in Figure 3a (after ~8 kA h of charge throughput). Further identification of the causes of degradation can be achieved through analysis of the degradation modes.

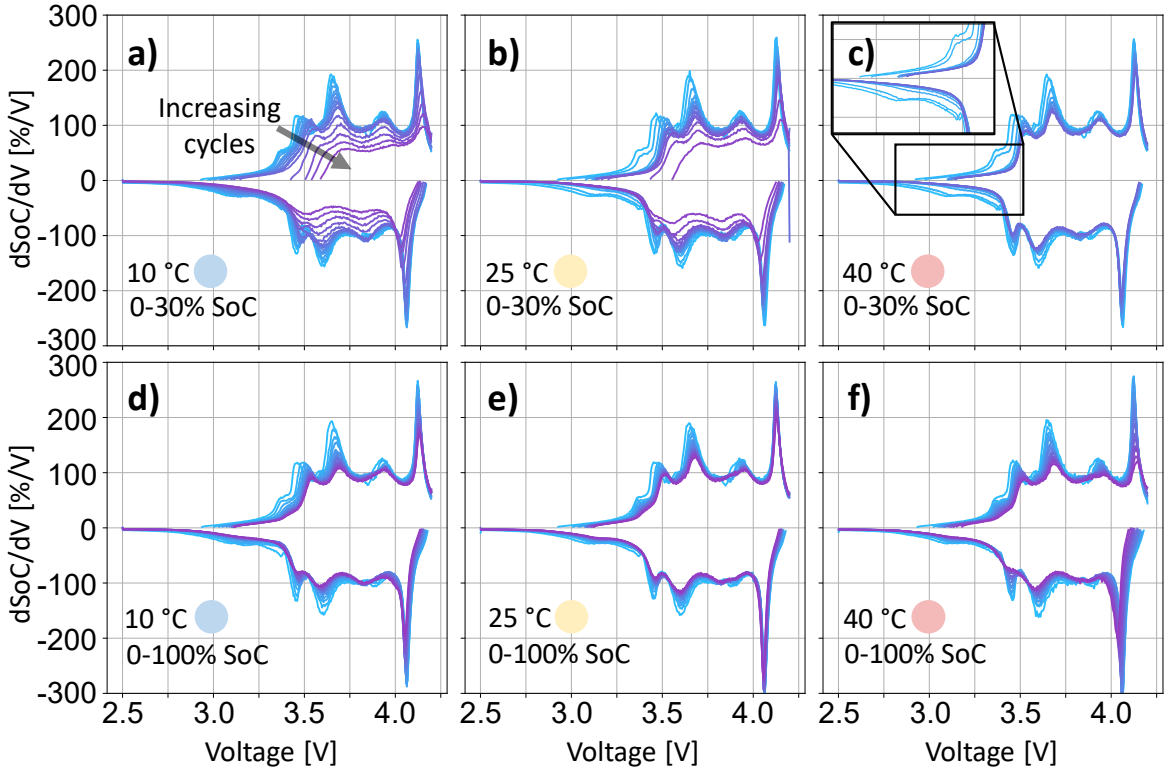

Figure 4: Incremental capacity analysis (ICA) progression throughout cell ageing. Data from cells aged at 0-30% SoC (a-c) and 0-100% SoC (d-f), at temperatures of 10°C (a,d), 25°C (b,e), and 40°C (c,f). ICA calculated from the 0.1C discharge-charge cycle, with a fixed dV value of 5 mV. Q values were normalised by the nominal BoL capacity (5 A h) to give 'SoC'. Different colours correspond to each RPT value, from BoL (light blue) to EoL (dark purple), with approximately 77 full equivalent cycles between each consecutive RPT.

DM analysis of each cell was performed as outlined in the experimental section, using the 0.1C

discharge data from the RPTs. The OCV-fitting procedure performed for each RPT allows us to calculate the capacities of the PE and NE and their relative offset, as well as the relative ratio of Gr:Si in the NE. By repeating the OCV-fitting at each point along the SoH of the cell, we can track the evolution of the DMs as a function of charge throughput. This includes LLI, and LAM of each electrode (LAM-PE and LAM-NE) as well as the LAM of each component of the NE (LAM-Gr and LAM-Si). It should be noted that this analysis cannot distinguish between loss of lithiated active material, and loss of delithiated active material alongside LLI. The calculated LLI could therefore be caused by either stoichiometric drift (i.e. 'electrode slippage') due to mechanisms such as SEI formation, or due to the LAM being lithiated material. Values of LLI have been normalised by dividing by the BoL cell capacity.

The results from the DM analysis of cells aged by cycling within different SoC windows and temperatures are displayed in **Error! Reference source not found.**. In these plots, multiple cells aged

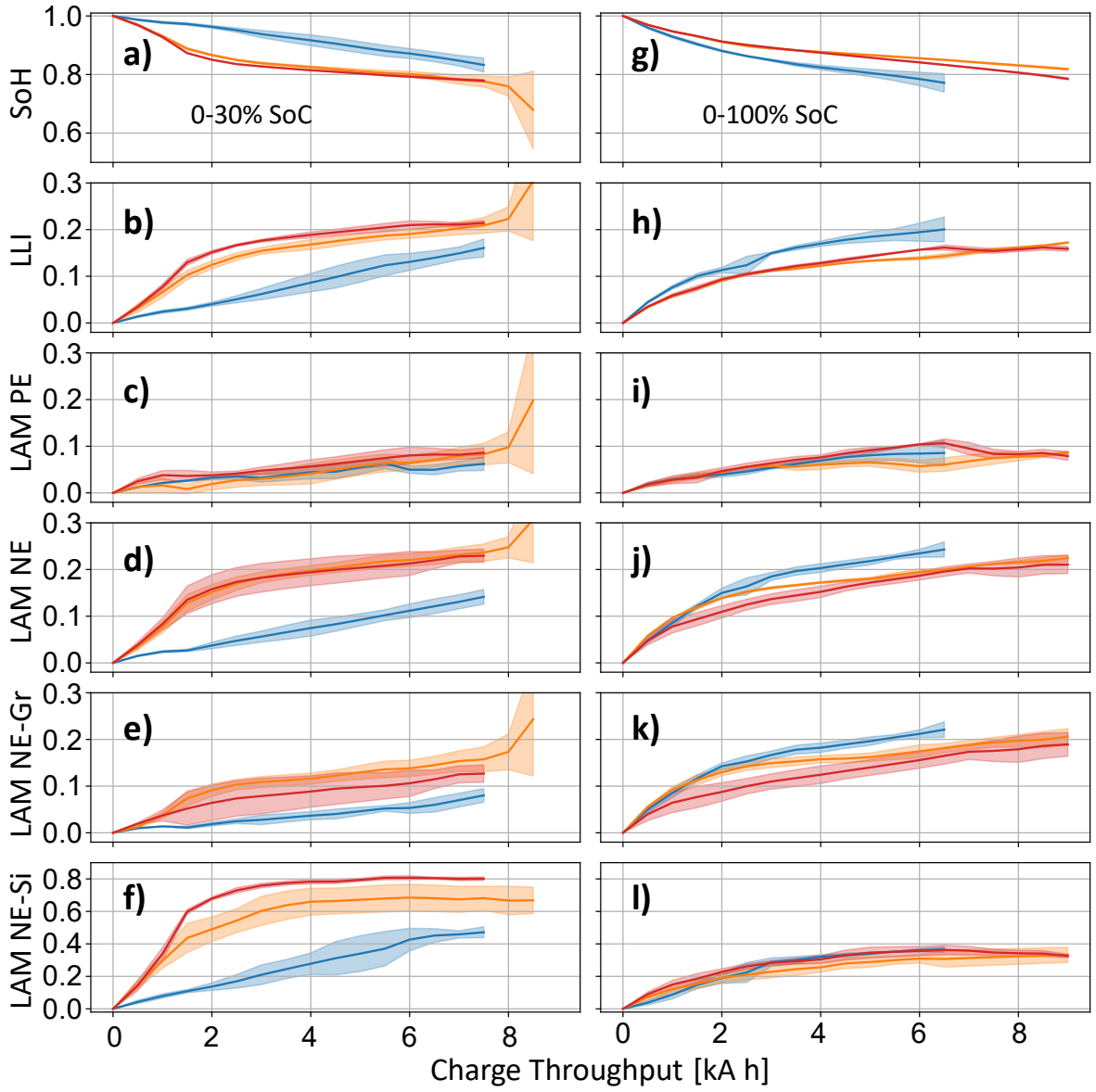

Figure 5: Degradation mode analysis for cells cycled at SoC ranges of 0-30% (a-f), and 0-100% (g-l). Colours correspond to cells aged at temperatures of 10°C (blue), 25°C (orange), and 40°C (red). Solid lines represent the average values calculated from multiple cells aged under the same condition, with shaded regions corresponding to the standard deviations. These plots show the evolution of SoH (cell capacity) and each degradation mode as a function of charge throughput during ageing. LLI has been normalised by the BoL capacity of the cell.

under the same conditions have been averaged to give the solid lines shown, with the shaded regions corresponding to the standard deviation. Results for each individual cell can be seen in SI Figures S11 and S13. In most cases, the root-mean-square error (RMSE) of the residual between the fitted OCV curve and the measured 0.1C data was found to be between 5-15 mV, with a gradual increase from BoL to EoL. This trend is expected due to the increasing resistance of the cells, causing the 0.1C discharge voltage to stray further away from the OCV.

Comparing the cells cycled over the 0-30% SoC range (Fig. 5a-f) with those cycled between 0-100% SoC (Fig. 5g-l) reveals significant differences in the DMs for the two operating ranges, in particular for LAM-Si. For the cells aged at low SoC and mid/high temperature (Fig. 5f), there is a greater than 70% loss in Si capacity after the first 4 kA h of energy throughput. This is expected, since the majority of the charge throughput in the 0-30% SoC range has been spent (de)lithiating silicon. Conversely, a greater proportion of the charge throughput in the 0-100% SoC range contributes towards (de)lithiating graphite, leading to higher levels of LAM-Gr in those cells (Fig. 5k). LAM-Gr also rises in the 0-30% SoC cells once the silicon content is rendered inactive, since the graphite is now cycled exclusively (Fig. 5e).

An appreciable amount of LAM-Si is also observed in the cells aged over the 0-100% SoC range, for which both the Si and Gr components are electrochemically cycled (note the different y-scales for LAM-Si and LAM-Gr on Figure 5). The high degree of LAM-Si relative to LAM-Gr may be caused by a variety of reasons: firstly, that the rate of Si degradation is inherently faster than that of Gr, in part due to the large volume changes experienced by Si upon (de)lithiation; secondly, due to the fact that the silicon particles experience far greater current densities than the graphite particles.[43] This is an unavoidable problem faced by composite electrodes, resulting from the fact that the electrochemically active surface area of Si is significantly smaller than that of Gr for the material ratios usually used. Higher current densities lead to larger concentration gradients and increased rates of degradation. This effect worsens as LAM-Si increases, since the active surface area of silicon consequently decreases.

There is also a strong temperature dependence observed for the LAM-Si when cycling within the 0-30% SoC range (Fig. 5f). Cells cycled at 10°C show lower levels of LAM-Si than those aged at 25°C or 40°C; they also have lower levels of LLI (Fig. 5b). This may indicate that the increased rates of SEI growth expected at higher temperatures have a knock-on effect on the LAM, which is primarily caused by particle cracking. Thicker SEI layers can hinder diffusion processes, leading to larger concentration gradients and increased particle cracking. It is also possible that the low temperatures, and resultant large overpotentials on the silicon active material, cause the graphite to take on a larger portion of the charge throughput. These characteristics are expected to depend on the relative overpotentials of the two active materials, which depend on material properties and particle sizes, and should be the focus of future work.

The temperature dependence of the LAM-Gr in the 0-100% SoC cells (Fig. 5k) appears to be non-linear; the highest levels of LAM-Gr are observed in the cells aged at 10°C, whilst those aged at 25°C and 40°C show similar levels of material loss. This indicates that the kinetic limitations which cause high levels of particle cracking in Gr are abated by operating at temperatures of 25°C and above.

Finally, similar levels of LAM-PE are observed in all cells tested here, regardless of the SoC range or temperature that the cells were cycled over (Fig. 5c & i). This suggests that the degradation mechanisms responsible for the observed LAM-PE are not SoC-dependent, which would indicate the dominant mechanism being particle cracking. Other PE degradation mechanisms, such as structural

disordering, phase change and oxidation of the lattice oxygen, are expected to be exacerbated by higher cell SoCs and temperatures.

Conclusions

We have investigated the effects of state-of-charge (SoC) and temperature on the degradation of commercial lithium-ion batteries with Si-Gr/NMC811 electrodes. We found that cycling at low SoC causes greater rates of capacity fade at 25/40°C, but appears to have the opposite effect at 10°C. Similar trends were observed for the increase in ohmic resistance, indicating that the mechanisms affecting these two metrics were linked.

By using a form of open circuit voltage modelling which utilises separate negative electrode (NE) voltage curves for silicon and graphite, we were able to quantify the relative capacities of these two components, which were calculated as 85:15 (Gr:Si) at beginning-of-life. This methodology was then used to track the evolution of different degradation modes (DMs) during battery aging, giving quantitative values of loss of active material for both Si (LAM-Si) and Gr (LAM-Gr), as well as loss of active material in the positive electrode (LAM-PE) and loss of lithium inventory (LLI).

The DM analysis revealed vast amounts of LAM-Si during cycling, particularly for the cells cycled at low SoC and high temperature. Once the Si content of the NE was rendered inactive, LAM-Gr was observed to rise, since the graphite was now providing the bulk of the electrochemical work. Similarly, operating the cells over the full 0-100% SoC range, where both the Gr and Si components are electrochemically cycled, resulted in less LAM-Si and more LAM-Gr compared to the low SoC ageing. LAM-PE was found to be similar in all operating conditions in these experiments, and thus independent of SoC range and temperature. This is expected at the relatively low charging currents and when adhering to the manufacturer's upper voltage limits.

The results of the DM analysis performed in this work question the utility of silicon in these commercial cells. Silicon capacity loss of over 30% was observed after just 5 kA h of charge throughput, even when cycling under moderate conditions (0-100% SoC, 25°C). For the same charge throughput, the loss in Si capacity was a staggering 80% when cycling over the 0-30% SoC range. These results indicate that the cycle life of cells containing Si-Gr NEs can be extended by reducing the amount of charge passed in the low SoC region. However, limiting the operational SoC window reduces the usable capacity of the cell, potentially removing the benefit of incorporating silicon into the electrode.

The degradation mode analytical method used here provides greater insight into the observed ageing behaviour by decoupling the LAM contributions from the two components of the NE. This methodology provides a suitable framework for analysis of other experimental degradation studies on cells containing composite electrodes.

Supporting Information

Supporting Information is available in a separate document.

Acknowledgements

The authors would like to thank Tom Cleaver and M. Waseem Marzook from Cognition Energy for their help in the design of the test apparatus, and Carlos Garcia and Karthik Radhakrishnan for aiding with the experiments.

This work was kindly supported by the Innovate UK WIZer project (grant number 104427) and EPSRC Faraday Institution Multi-Scale Modelling project (https://faraday.ac.uk/; EP/S003053/1, grant number FIRG003).

CRediT author statements

N.K.: Conceptualisation, Methodology, Investigation, Formal analysis, Data Curation, Writing - Original Draft, Visualisation

M.A.S.: Methodology, Investigation, Writing – Review & Editing, Visualisation

G.J.O.: Conceptualisation, Writing – Review & Editing, Supervision, Funding acquisition

M.M.: Conceptualisation, Writing – Review & Editing, Supervision, Funding acquisition

Y.P.: Conceptualisation, Methodology, Writing – Review & Editing, Supervision, Funding acquisition

Conflict of Interest

The authors have no conflict of interest to declare.

1. Bloomberg NEF. *Electric Vehicle Outlook*. https://about.bnef.com/electric-vehicle-outlook/ (2021).

2. IEA. *Innovation in Batteries and Electricity Storage*. https://www.iea.org/reports/innovation-in-batteries-and-electricity-storage (2020).

3. Obrovac, M. N. & Christensen, L. Structural changes in silicon anodes during lithium insertion/extraction. *Electrochem. Solid-State Lett.* **7**, A93 (2004).

4. Beaulieu, L. Y., Hatchard, T. D., Bonakdarpour, A., Fleischauer, M. D. & Dahn, J. R. Reaction of Li with Alloy Thin Films Studied by In Situ AFM. *J. Electrochem. Soc.* **150**, A1457 (2003).

5. Prado, A. Y. R., Rodrigues, M.-T. F., Trask, S. E., Shaw, L. & Abraham, D. P. Electrochemical Dilatometry of Si-Bearing Electrodes: Dimensional Changes and Experiment Design. *J. Electrochem. Soc.* **167**, 160551 (2020).

6. Kumar, R. *et al.* In Situ and Operando Investigations of Failure Mechanisms of the Solid Electrolyte Interphase on Silicon Electrodes. *ACS Energy Lett.* **1**, 689–697 (2016).

7. Li, X. *et al.* Degradation mechanisms of high capacity 18650 cells containing Si-graphite anode and nickel-rich NMC cathode. *Electrochim. Acta* **297**, 1109–1120 (2019).

8. Klett, M. *et al.* Electrode Behavior RE-Visited: Monitoring Potential Windows, Capacity Loss, and Impedance Changes in Li 1.03 (Ni 0.5 Co 0.2 Mn 0.3) 0.97 O 2 /Silicon-Graphite Full Cells . *J. Electrochem. Soc.* **163**, A875–A887 (2016).

9. McBrayer, J. D. *et al.* Calendar aging of silicon-containing batteries. *Nature Energy* vol. 6 866–872 (2021).

10. Eshetu, G. G. *et al.* Production of high-energy Li-ion batteries comprising silicon-containing anodes and insertion-type cathodes. *Nature Communications* vol. 12 1–14 (2021).

11. Cunningham, B. *Silicon and Intermetallic Anode Portfolio Strategy Overview*. (2020).

12. Kim, T., Park, S. & Oh, S. M. Solid-State NMR and Electrochemical Dilatometry Study on Li[sup +] Uptake/Extraction Mechanism in SiO Electrode. *J. Electrochem. Soc.* **154**, A1112 (2007).

13. Li, H. *et al.* SiO $_x$ Anode: From Fundamental Mechanism toward Industrial Application. *Small* 2102641 (2021) doi:10.1002/smll.202102641.

14. Kitada, K. *et al.* Unraveling the Reaction Mechanisms of SiO Anodes for Li-Ion Batteries by Combining in Situ 7Li and ex Situ 7Li/29Si Solid-State NMR Spectroscopy. *J. Am. Chem. Soc.* **141**, 7014–7027 (2019).

15. Chae, S., Kim, N., Ma, J., Cho, J. & Ko, M. One-to-One Comparison of Graphite-Blended Negative Electrodes Using Silicon Nanolayer-Embedded Graphite versus Commercial Benchmarking Materials for High-Energy Lithium-Ion Batteries. *Adv. Energy Mater.* **7**, 1700071 (2017).

16. Klett, M., Gilbert, J. A., Pupek, K. Z., Trask, S. E. & Abraham, D. P. Layered Oxide, Graphite and Silicon-Graphite Electrodes for Lithium-Ion Cells: Effect of Electrolyte Composition and Cycling Windows. *J. Electrochem. Soc.* **164**, A6095–A6102 (2017).

17. Yao, K. P. C., Okasinski, J. S., Kalaga, K., Almer, J. D. & Abraham, D. P. Operando Quantification of (De)Lithiation Behavior of Silicon–Graphite Blended Electrodes for Lithium-Ion Batteries. *Adv. Energy Mater.* **9**, (2019).

18. Edge, J. S. *et al.* Lithium ion battery degradation: what you need to know. *Physical Chemistry Chemical Physics* vol. 23 8200–8221 (2021).

19. Lim, J. M. *et al.* Intrinsic Origins of Crack Generation in Ni-rich LiNi0.8Co0.1Mn0.1O2 Layered Oxide Cathode Material. *Sci. Rep.* **7**, 2–11 (2017).

20. Jung, R., Strobl, P., Maglia, F., Stinner, C. & Gasteiger, H. A. Temperature Dependence of Oxygen Release from LiNi 0.6 Mn 0.2 Co 0.2 O 2 (NMC622) Cathode Materials for Li-Ion Batteries. *J. Electrochem. Soc.* **165**, A2869–A2879 (2018).

21. Waldmann, T., Wilka, M., Kasper, M., Fleischhammer, M. & Wohlfahrt-Mehrens, M. Temperature dependent ageing mechanisms in Lithium-ion batteries - A Post-Mortem study. *J. Power Sources* **262**, 129–135 (2014).

22. Fan, J. & Tan, S. Studies on Charging Lithium-Ion Cells at Low Temperatures. *J. Electrochem. Soc.* **153**, A1081 (2006).

23. Ai, W., Kraft, L., Sturm, J., Jossen, A. & Wu, B. Electrochemical Thermal-Mechanical Modelling of Stress Inhomogeneity in Lithium-Ion Pouch Cells. *J. Electrochem. Soc.* **167**, 013512 (2020).

24. Henschel, J. *et al.* Lithium ion battery electrolyte degradation of field-tested electric vehicle battery cells – A comprehensive analytical study. *J. Power Sources* **447**, 227370 (2020).

25. Dubarry, M., Svoboda, V., Hwu, R. & Yann Liaw, B. Incremental Capacity Analysis and Close-to-Equilibrium OCV Measurements to Quantify Capacity Fade in Commercial Rechargeable Lithium Batteries. *Electrochem. Solid-State Lett.* **9**, A454 (2006).

26. Dubarry, M. & Liaw, B. Y. Identify capacity fading mechanism in a commercial LiFePO4 cell. *J. Power Sources* **194**, 541–549 (2009).

27. Birkl, C. R., Roberts, M. R., McTurk, E., Bruce, P. G. & Howey, D. A. Degradation diagnostics for lithium ion cells. *J. Power Sources* **341**, 373–386 (2017).

28. Birkl, C. R., McTurk, E., Roberts, M. R., Bruce, P. G. & Howey, D. A. A Parametric Open Circuit Voltage Model for Lithium Ion Batteries. *J. Electrochem. Soc.* **162**, A2271–A2280 (2015).

29. Prosser, R., Offer, G. & Patel, Y. Lithium-Ion Diagnostics: The First Quantitative In-Operando Technique for Diagnosing Lithium Ion Battery Degradation Modes under Load with Realistic Thermal Boundary Conditions. *J. Electrochem. Soc.* **168**, 030532 (2021).

30. Dubarry, M. *et al.* Evaluation of commercial lithium-ion cells based on composite positive electrode for plug-in hybrid electric vehicle applications. Part II. Degradation mechanism under 2 C cycle aging. *J. Power Sources* **196**, 10336–10343 (2011).

31. Dubarry, M., Truchot, C. & Liaw, B. Y. Synthesize battery degradation modes via a diagnostic and prognostic model. *J. Power Sources* **219**, 204–216 (2012).

32. Bloom, I. *et al.* Differential voltage analyses of high-power, lithium-ion cells 1. Technique and application. *J. Power Sources* **139**, 295–303 (2005).

33. Bloom, I., Christophersen, J. P., Abraham, D. P. & Gering, K. L. Differential voltage analyses of high-power lithium-ion cells: 3. Another anode phenomenon. *J. Power Sources* **157**, 537–542 (2006).

34. Bloom, I. *et al.* Differential voltage analyses of high-power lithium-ion cells. 4. Cells containing NMC. *J. Power Sources* **195**, 877–882 (2010).

35. Ando, K., Matsuda, T. & Imamura, D. Degradation diagnosis of lithium-ion batteries with a LiNi0.5Co0.2Mn0.3O2 and LiMn2O4 blended cathode using dV/dQ curve analysis. *J. Power Sources* **390**, 278–285 (2018).

36. Anseán, D. *et al.* Mechanistic investigation of silicon-graphite/LiNi0.8Mn0.1Co0.1O2 commercial cells for non-intrusive diagnosis and prognosis. *J. Power Sources* **459**, 227882 (2020).

37. Schmitt, J., Schindler, M. & Jossen, A. Change in the half-cell open-circuit potential curves of silicon–graphite and nickel-rich lithium nickel manganese cobalt oxide during cycle aging. *J. Power Sources* **506**, 230240 (2021).

38. Zilberman, I., Sturm, J. & Jossen, A. Reversible self-discharge and calendar aging of 18650 nickel-rich, silicon-graphite lithium-ion cells. *J. Power Sources* **425**, 217–226 (2019).

39. Wang, C. *et al.* Cold Ageing of NMC811 Lithium-ion Batteries. *Energies* **14**, 4724 (2021).

40. Krause, F. C. *et al.* Performance of Commercial Li-Ion Cells for Future NASA Missions and Aerospace Applications. *J. Electrochem. Soc.* **168**, 040504 (2021).

41. Kyle William Butterfield, Tyler David Collins & Nathaniel Christopher Wynn. Cylindrical Battery Cell Packaging and Cooling Configuration. (2018).

42. Chen, C.-H. *et al.* Development of Experimental Techniques for Parameterization of Multi-scale Lithium-ion Battery Models. *J. Electrochem. Soc.* **167**, 80534 (2020).

43. Ai, W. *et al.* A composite electrode model for lithium-ion batteries with silicon/graphite negative electrodes. *J. Power Sources* **527**, 231142 (2022).